
Probabilistic Contrastive Learning with Explicit Concentration on the Hypersphere

Hongwei Bran Li

Athinoula A. Martinos Center
MGH, HMS, Harvard University
holi2@mgh.harvard.edu

Cheng Ouyang

Imperial College London
c.ouyang@imperial.ac.uk

Tamaz Amiranashvili

Technical University of Munich
tamaz.amiranashvili@uzh.ch

Matthew S. Rosen

Athinoula A. Martinos Center
MGH, HMS, Harvard University
msrosen@mgh.harvard.edu

Bjoern Menze

University of Zurich
bjoern.menze@uzh.ch

Juan Eugenio Iglesias

Athinoula A. Martinos Center
MGH, HMS, Harvard University
jei@mit.edu

Abstract

Self-supervised contrastive learning has predominantly adopted deterministic methods, which are not suited for environments characterized by uncertainty and noise. This paper introduces a new perspective on incorporating uncertainty into contrastive learning by embedding representations within a spherical space, inspired by the von Mises-Fisher distribution (vMF). We introduce an unnormalized form of vMF and leverage the concentration parameter, κ , as a direct, interpretable measure to quantify uncertainty *explicitly*. This approach not only provides a probabilistic interpretation of the embedding space but also offers a method to calibrate model confidence against varying levels of data corruption and characteristics. Our empirical results demonstrate that the estimated concentration parameter correlates strongly with the degree of unforeseen data corruption encountered at test time, enables failure analysis, and enhances existing out-of-distribution detection methods.

1 Introduction

Self-supervised contrastive learning has significantly narrowed the gap between unsupervised and supervised learning across various domains, including vision [7, 8, 5, 51] and multimodal learning [15]. Despite these notable achievements, current methods still fall short in critical aspects necessary for decision-making in high-stakes applications. In domains such as medical diagnosis [1] and autonomous driving [24], where decisions can have serious consequences, accurately estimating uncertainty, especially aleatoric uncertainty inherent to data, is essential.

Traditional contrastive learning methods are predominantly *deterministic* and lack mechanisms to gauge uncertainty, limiting their utility in scenarios where understanding the model's confidence is crucial. Previous attempts to incorporate uncertainty estimation have primarily utilized Gaussian distributions [27, 11, 44], which may not align well with hyperspherical contrastive representations [2, 43, 17, 8]. Recent research has begun exploring geometric properties of contrastive

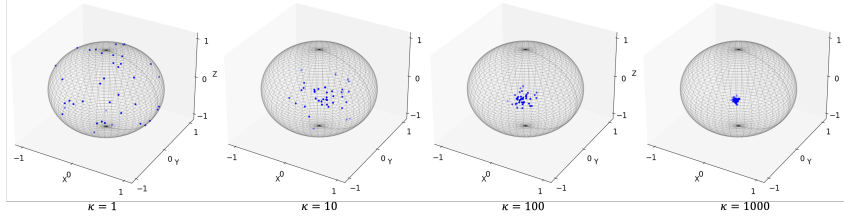


Figure 1: The von Mises-Fisher (vMF) distribution with a fixed mean vector and varied concentration values κ on a sphere. Our framework equips contrastive learning representations to have the vMF distribution and utilizes the estimated κ 's as the indications of uncertainty.

representations [48, 46, 13], prompting a shift towards probabilistic models better suited to these spaces.

Consequently, we turn our attention to the von Mises-Fisher (vMF) distribution [10], a distribution adept at handling data on the sphere, thus aligning more closely with the intrinsic structure of most contrastive learning representations. The vMF distribution is parameterized by a mean direction μ and a concentration parameter κ . The κ controls the spread of the distribution: when κ is high, the distribution is highly concentrated around μ . As shown in Figure 1, this concentration means that the points sampled from the distribution are closely clustered around the mean, indicating lower dispersion. Therefore, κ can be viewed as a measure of uncertainty.

Recent advancements, such as the formulation proposed by [29], have integrated Monte Carlo sampling with the contrastive loss, facilitating an *implicit* learning of κ . However, this approach encourages the κ values of paired positive samples to be similar, is not input-dependent, and does not capture *explicit* uncertainty. In reality, aleatoric uncertainty varies across different instances x reflecting in distinct generative distributions $p(y|x)$. In this work, we propose a novel probabilistic contrastive learning approach to model uncertainty by integrating the vMF distribution. Our probabilistic embedding alignment loss enforces κ as a purely *input-dependent* parameter, allowing our method to estimate the inherent uncertainty of each data point, leading to more reliable uncertainty estimation.

In summary, **(1)** we propose a vMF -inspired probabilistic contrastive learning framework that captures uncertainty in hyperspherical spaces. **(2)** We develop an embedding alignment loss accounting for direction and concentration, compatible with existing contrastive learning methods while maintaining representation discriminativeness. **(3)** We empirically demonstrate our framework's effectiveness in quantifying degrees of corruption and failure analysis during test time and potential in enhancing the representations for out-of-the-distribution (OOD) detection.

2 Method

2.1 Preliminaries on Contrastive Learning and the von Mises-Fisher Distribution

Contrastive learning learns to encode semantically similar data points close together and dissimilar points far apart in an embedding space in a *deterministic* fashion. A common approach involves positive and negative pairs: given a data point x , two augmented views x_i and x_j are created. The objective is to maximize the similarity of these views (positive pairs) while minimizing the similarity with other data points (negative pairs). This can be formalized using a loss function like the widespread *SimCLR* framework [7]. Its contrastive loss is formulated as:

$$\mathcal{L}_{\text{contrastive}} = -\log \frac{\exp(\text{sim}(z_i, z_j)/\tau)}{\sum_{k=1}^N \exp(\text{sim}(z_i, z_k)/\tau)}, \quad (1)$$

where z_i and z_j are the representations of x_i and x_j in embedding space, $\text{sim}(\cdot)$ is a similarity measure (typically the *cosine similarity*), τ is a temperature scaling parameter, and the sum in the denominator is over one positive and $N - 1$ negative pairs.

The vMF distribution [10] is a distribution on the unit sphere in \mathbb{R}^n to model data points on an n -dimensional hypersphere, making it suitable for spherical embedding spaces. Its probability density function is:

$$p(x; \mu, \kappa) = C(\kappa) \exp(\kappa \mu^T x), \quad (2)$$

where \mathbf{x} is a point on the unit sphere, $\boldsymbol{\mu}$ is the mean direction, κ is the scalar concentration parameter, and $C(\kappa) = \kappa^{n/2-1} (2\pi)^{-n/2} / I_{n/2-1}(\kappa)$ is the normalization constant that ensures integration to one; I_ν is the modified Bessel function [49] of the first kind at order ν . The concentration parameter κ determines the dispersion of the distribution around the mean direction $\boldsymbol{\mu}$. A higher κ indicates less dispersion (more concentration around the mean), whereas a lower κ indicates more dispersion.

There is an **overflow issue** in vMF distribution, which arises due to the calculation of the normalization constant $C(\kappa)$ [3]. The modified Bessel function of the first kind $I_\nu(\kappa)$ grows exponentially with increasing κ , especially in high-dimensional spaces where the order $\nu = \frac{n}{2} - 1$ can be large. This rapid growth can lead to numerical overflow, where the function values exceed the maximum representable value in floating-point arithmetic. Such an overflow issue can disrupt the stability and accuracy of computations, particularly during the training of models using gradient-based optimization methods.

2.2 Unnormalized vMF Distribution with a Regularization

An unnormalized and simplified form. To circumvent the overflow issue discussed above, we consider an unnormalized form of the vMF distribution that omits the normalization constant and focuses on the core exponential term:

$$\psi(\mathbf{x}; \boldsymbol{\mu}, \kappa) = \exp(\kappa \boldsymbol{\mu}^\top \mathbf{x}) \quad (3)$$

This unnormalized form simplifies our model, making it computationally more efficient and stable, while still capturing the essential directional and concentration properties of the data. Although the unnormalized vMF is unbounded (for large kappa) and does not yield true probabilities, it is in practice an effective contrastive learning objective – since it relies on relative comparisons rather than absolute values. The normalization constant $C(\kappa)$ for the vMF distribution inherently favors smaller values of κ due to its mathematical properties. Specifically, the term in the log-likelihood acts as a natural regularizer on κ , encouraging the distribution to avoid extreme concentration and maintain a degree of uncertainty. However, removing $C(\kappa)$ necessitates an alternative technique to mimic this regularization effect. Below, we perform an analysis and propose a ℓ_2 regularization on κ .

Analysis on a regularization on κ . Consider the log-likelihood function of the vMF distribution for a data point \mathbf{x} on the unit sphere with mean direction $\boldsymbol{\mu}$ and concentration parameter κ :

$$\mathcal{L}(\boldsymbol{\mu}, \kappa) = \log p(\mathbf{x}; \boldsymbol{\mu}, \kappa) = \log C(\kappa) + \kappa \boldsymbol{\mu}^\top \mathbf{x} \quad (4)$$

The normalization constant $C(\kappa)$ involves the modified Bessel function $I_{p/2-1}(\kappa)$, which grows exponentially with κ . The term $\log C(\kappa)$ in the log-likelihood acts as a natural penalty on κ :

$$\log C(\kappa) = (p/2 - 1) \log \kappa - \log I_{p/2-1}(\kappa) - \frac{p}{2} \log(2\pi) \quad (5)$$

For large κ , $I_{p/2-1}(\kappa) \approx \frac{e^\kappa}{\sqrt{2\pi\kappa}}$, thus:

$$\log C(\kappa) \approx (p/2 - 1) \log \kappa - \kappa - \log(\sqrt{2\pi\kappa}) \quad (6)$$

This approximation shows that $\log C(\kappa)$ introduces a term $-\kappa$, which effectively penalizes large κ values. The $-\log(\sqrt{2\pi\kappa})$ term contributes a smaller additional penalty. By introducing ℓ_2 regularization, we can mimic this penalization:

$$\mathcal{L}_{\text{reg}} = -\lambda \kappa^2 \quad (7)$$

Here, λ is a regularization parameter controlling the strength of the penalty. In high-dimensional spaces, large κ values can cause numerical instability due to the exponential terms in the vMF distribution. ℓ_2 regularization on κ helps maintain stability by keeping κ values moderate, ensuring that gradients do not explode during optimization.

Probabilistic interpretation. From a Bayesian perspective, regularization can be interpreted as placing a prior on the parameter. An ℓ_2 regularization term corresponds to a Gaussian prior on κ :

$$P(\kappa) \propto \exp(-\lambda \kappa^2) \quad (8)$$

This prior assumes that κ takes smaller values, aligning with the nature of the vMF distribution to avoid extreme concentrations.

2.3 Probabilistic Contrastive Learning on the Hypersphere

Unit sphere normalization. First, we enhance the sensitivity of the contrastive learning representation to angular differences by projecting each data point \mathbf{x} onto the unit sphere, defined as: $\mathbf{z} = f(\mathbf{x})/\|f(\mathbf{x})\|$, where $f(\mathbf{x})$ is the representation obtained with an encoder network $f(\cdot)$, and $\|f(\mathbf{x})\|$ is its Euclidean norm. This mapping to the unit sphere ensures that all comparisons between embeddings are based solely on their directionality, which is inherently measured by cosine similarity in existing contrastive learning [7, 8, 14], aligning perfectly with our geometric constraints.

Then, we incorporate the vMF distribution into a contrastive learning framework that leverages this hyperspherical embedding. The vMF distribution is ideally suited for embeddings that are normalized in this manner and provide a probabilistic interpretation of the dispersion of points around a mean direction.

Probabilistic embedding alignment. We leverage the directional consistency between data pairs and enforce κ to be a purely *input-dependent* parameter.

Let \mathbf{x} be an input image batch from a training set. Two augmented views of \mathbf{x} , denoted as \mathbf{x}_1 and \mathbf{x}_2 , are generated using a predefined augmentation pipeline. This pipeline typically includes transformations such as random cropping, resizing, color jittering, and horizontal flipping [7].

A neural network model $f(\cdot)$ processes each augmented view and outputs an d -dimensional mean directional vector $\boldsymbol{\mu}'$ and a scalar concentration parameter κ . Let $\boldsymbol{\mu}$ be the normalized vector: $\boldsymbol{\mu} = \boldsymbol{\mu}'/\|\boldsymbol{\mu}'\|$. The embedding spaces are then represented as $(\boldsymbol{\mu}_1, \kappa_1) = f(\mathbf{x}_1)$ and $(\boldsymbol{\mu}_2, \kappa_2) = f(\mathbf{x}_2)$, where κ_1 and κ_2 are non-negative.

In the contrastive learning context, we propose a *probabilistic embedding alignment loss* for the distributions of two augmented views (positive pairs). The alignment of $\boldsymbol{\mu}_2$ given $(\boldsymbol{\mu}_1, \kappa_1)$ and $\boldsymbol{\mu}_1$ given $(\boldsymbol{\mu}_2, \kappa_2)$ can be formulated as:

$$\mathcal{L}_a(\boldsymbol{\mu}_1, \kappa_1, \boldsymbol{\mu}_2, \kappa_2) = \exp[(\kappa_1 + \kappa_2) \cdot \boldsymbol{\mu}_1^T \boldsymbol{\mu}_2] \propto \exp(\kappa_1 \cdot \cos(\theta)) \cdot \exp(\kappa_2 \cdot \cos(\theta)), \quad (9)$$

where θ is the angle between $\boldsymbol{\mu}_1$ and $\boldsymbol{\mu}_2$, and $\cos(\theta)$ can be computed as the dot product between $\boldsymbol{\mu}_1$ and $\boldsymbol{\mu}_2$ due to their normalization. The loss is then defined as the negative log-alignment:

$$\mathcal{L}_{\text{align}} = -\lambda_{\text{align}} \cdot (\kappa_1 + \kappa_2) \boldsymbol{\mu}_1^T \boldsymbol{\mu}_2, \quad (10)$$

where λ_{align} controls the strength of the loss. This loss emphasizes the exponential alignment of embeddings based on their dot product, scaled by the sum of their concentration parameters. Unlike the *MC-InfoNCE* loss [29], our loss *directly* links the strength of the alignment to the uncertainty of the embeddings, as represented by κ . Intuitively, the alignment loss encourages the encoder to learn embeddings with a desired property: the mean directions $\boldsymbol{\mu}_1$ and $\boldsymbol{\mu}_2$ are closely aligned when the representations are certain (i.e., high κ values) while treating κ_1 and κ_2 as variables capturing different degrees of uncertainties. Hence, it relaxes the unrealistic assumption that κ values from positive pairs are expected to be *similar* as in previous work [29]. We provide an analysis on the gradient behavior of Eq. 10 in the Appendix.

Note that, due to the unnormalized vMF distribution, the loss in Eq. 10 can be infinitely small if κ_1 and κ_2 grow unboundedly. Therefore, as discussed in Sec. 2.2, we regularize κ by an ℓ_2 -norm regularization loss:

$$\mathcal{L}_{\text{reg}}(\kappa_1, \kappa_2) = \lambda_{\text{reg}} \cdot (\kappa_1^2 + \kappa_2^2), \quad (11)$$

where λ_{κ} is a hyperparameter that controls the strength of the regularization.

The final loss. To maintain the discriminativeness of the embeddings, we employ the original deterministic contrastive loss applied to the mean direction vectors from positive pairs and negative pairs, computed using Eq. 1. We combine the proposed *embedding alignment* loss, the ℓ_2 -norm regularization, and the *SimCLR* contrastive loss [7]:

$$\mathcal{L}_{\text{total}} = \mathcal{L}_{\text{align}}(\kappa_1, \kappa_2) + \mathcal{L}_{\text{reg}}(\kappa_1, \kappa_2) + \mathcal{L}_{\text{contrastive}}(\mathbf{x}_1, \mathbf{x}_2). \quad (12)$$

This combined loss function enables the model to learn uncertainty-aware and discriminative embeddings. Notably, our proposed alignment loss requires only positive pairs, making it plug-and-play compatible with most contrastive learning methods. The optimization is detailed in Algorithm 1.

Algorithm 1 Probabilistic Contrastive Learning with Embedding Alignment

```
1: for each batch  $\{\mathbf{x}^i\}_{i=1}^N$  do
2:    $\{(\mathbf{x}_1^i, \mathbf{x}_2^i)\}_{i=1}^N \leftarrow \text{Augment}(\{\mathbf{x}^i\}_{i=1}^N)$  % Get positive pairs via augmentations
3:   for each positive pair  $(\mathbf{x}_1, \mathbf{x}_2)$  in the batch do
4:      $(\boldsymbol{\mu}_1, \kappa_1), (\boldsymbol{\mu}_2, \kappa_2) \leftarrow f(\mathbf{x}_1), f(\mathbf{x}_2)$  % Get mean directions and concentrations
5:      $\kappa_1, \kappa_2 \leftarrow \text{Softplus}(\kappa_1, \kappa_2)$  % Ensure positive  $\kappa$  values
6:     Compute  $\mathcal{L}_{\text{align}}$  with Eq. 10
7:     Compute  $\mathcal{L}_{\text{contrastive}}$  using  $(\boldsymbol{\mu}_1, \boldsymbol{\mu}_2)$ 
8:      $\mathcal{L}_{\text{reg}}(\kappa) \leftarrow \lambda_{\kappa} \cdot (\kappa_1^2 + \kappa_2^2)$ 
9:      $\mathcal{L}_{\text{total}} \leftarrow \mathcal{L}_{\text{align}} + \mathcal{L}_{\text{contrastive}} + \mathcal{L}_{\text{reg}}$ 
10:    Backpropagate and update model parameters
11:   end for
12: end for
```

3 Related Work

Representation learning on the unit hypersphere has its advantages in representation quality and interpretability [39, 9]. Theoretical analysis has shown that such methods learn alignment and uniformity properties asymptotically on the hypersphere [48]. It has been therefore widely adopted by the popular contrastive learning approaches [2, 43, 17, 8]. Hyperspherical latent spaces in variational autoencoders have demonstrated superior performance over Euclidean counterparts [9, 50]. Hyperspherical face embeddings have outperformed their unnormalized counterparts [33, 47]. Recently, contrastive learning on the hypersphere has been shown effective in out-of-distribution detection [36]. The consistent empirical success across diverse applications and nice geometric properties underscores the hypersphere’s uniqueness as a feature space. In the context of our work, we extend this exploration to the realm of uncertainty estimation within these hyperspherical spaces.

Aleatoric uncertainty is inherent in many vision problems, such as object recognition [25, 42] and semantic segmentation [37, 22], where stochasticity in image acquisition (*e.g.*, noise and imaging artifacts) incurs uncertainties in prediction. Other tasks with ambiguous input data include 3D reconstruction from 2D input [6] or from noisy sensor [35]. To facilitate the systematic study of aleatoric uncertainty, the widely-applied benchmark proposed by [20] quantifies the severity of data corruptions (*e.g.*, imaging noise, distortions caused by compression, etc.) into different corruption levels [20]. In this work, we demonstrate that the estimated concentration parameters κ ’s closely *correlate* with the corruption levels.

Probabilistic embedding are emerging approaches that involve encoders generating distributions within the latent space, rather than deterministic point estimates. Such approaches to probabilistic embeddings diverge into two primary categories: The first method transforms traditional loss functions into probabilistic formats by aggregating the entire loss across the spectrum of predicted probabilistic embeddings [41, 40, 29]. Another strategy employs distribution-to-distribution metrics to substitute the conventional point-to-point distances in loss calculations, with the Expected Likelihood Kernel [42] standing out as a particularly effective technique. Notably, it has recently shown its efficacy even in contexts involving high-dimensional embedding spaces [28]. Recently, a Monte-Carlo sampling-based *InfoNCE* loss [29] was proposed to train the encoder to predict probabilistic embeddings and to learn the correct posteriors. In our work, we present a fresh perspective on modeling such a probabilistic embedding by introducing the unnormalized *vMF* and a regularization term, resulting in an effective and computationally efficient framework.

4 Experiments and Results

4.1 Experimental Setup

Quantifying the level of data corruption. CIFAR-10-C [19] is a well-established benchmark dataset for evaluating model robustness in a controlled environment. It contains 18 image corruption types based on the original CIFAR-10 [30]. Our key assumption is that the corrupted data have higher inherent aleatoric uncertainty compared to the uncorrupted one. We therefore assume that higher degrees of corruption would result in higher uncertainties (lower concentration κ). We use *Spearman*

Correlation as an evaluation metric to quantify if a model could capture this connection. We use the non-parametric, ranking-based Spearman correlation (rather than Pearson) as the relationship between the variables is highly nonlinear (i.e., we test for their monotonicity). Some corruptions are shown in Figure 2.

OOD detection. From CIFAR-10, CIFAR-100, and MNIST [32], we generate six in-domain and out-of-domain pairs for the OOD detection tasks, as shown in Table 2. Area Under the Receiver Operating Characteristic curve (AUROC) is used for the detection accuracy following the practice from [31]. For this task, we train three different models on the three domains from scratch. The learned κ is treated as a one-dimensional feature (or anomaly score) to enhance the features for OOD detection.

4.2 Baselines

To quantify the uncertainty in representations, we compare our method with the following baselines.

Model ensembles. We train multiple models and then evaluate the empirical variance in their representations. The variance among these models’ representations is used as a measure of uncertainty. Practically, each model in the ensemble can be trained with stochasticity (different initializations, etc.) on the same dataset or from different training epochs [21]. High variance indicates less certainty in the representations.

Let $f_{i,d}(x)$ denote the prediction of the i -th model in the ensemble for input x at the d -th feature. For an ensemble of M models and a feature dimension D , the average uncertainty $U_{\text{avg}}(x)$ for input x is given by: $U_{\text{avg}}(x) = \frac{1}{D} \sum_{d=1}^D \left(\frac{1}{M} \sum_{i=1}^M (f_{i,d}(x) - \bar{f}_d(x))^2 \right)$, where $\bar{f}_d(x)$ is the average prediction for input x at the d -th feature: $\bar{f}_d(x) = \frac{1}{M} \sum_{i=1}^M f_{i,d}(x)$.

Monte Carlo (MC) dropout [12] quantifies uncertainty by enabling dropout during inference and running multiple forward passes through the network which can be seen as sampling from an approximate posterior distribution of the model weights. The variance across these forward passes is used to estimate the uncertainty.

Let $g_{j,d}(x)$ represent the prediction of the model on the j -th forward pass with dropout for input x at the d -th feature. For N forward passes and feature dimension D , the average uncertainty $V_{\text{avg}}(x)$ for input x is: $V_{\text{avg}}(x) = \frac{1}{D} \sum_{d=1}^D \left(\frac{1}{N} \sum_{j=1}^N (g_{j,d}(x) - \bar{g}_d(x))^2 \right)$, where $\bar{g}_d(x)$ is the average prediction across the N forward passes for input x at the d -th feature: $\bar{g}_d(x) = \frac{1}{N} \sum_{j=1}^N g_{j,d}(x)$.

MCInfoNCE [29] involves an MC sampling process to model the probabilistic nature of embeddings via a reparametrization trick for vMF distribution [9]. This sampling process allows for the approximation of expectations over the latent space, which is essential in scenarios where direct calculation of these expectations is intractable. Since our method works with *SimCLR* contrastive loss, for a fair comparison, we adapt their *InfoNCE*-based [45] loss to the *SimCLR* contrastive loss and use the same architectures for the mean direction μ and κ . However, we still term it as *MC-InfoNCE* loss for literature consistency in the following experiments. The codes of the implementation are in Appendix D.

4.3 Training

Architecture. The encoder network contains two projection heads for the mean direction μ and κ based on *ResNet50* [18]. The projection head for the μ is realized through a sequential arrangement of layers, starting with a linear transformation from the 2048-dimensional *ResNet50* feature space to an intermediate 512-dimensional space, followed by batch normalization and *ReLU* activation, and finally projecting down to a d -dimensional representation. d is set to 128 for all experiments except the study on dimension in Table . In parallel, the κ parameter is estimated through a separate head, mirroring the structure but diverging in its final output to produce a single scalar value per input. κ is then passed through a *softplus* function [38], ensuring its non-negativity and adherence to the constraints of a concentration parameter in a probabilistic setting. The codes of the neural architecture are in Appendix E.

Table 1: **Spearman correlation between kappa values and the levels of corruption.** As the severity of corruption increases, κ decreases, implying higher uncertainty in the representations. + and - indicate that the correlations are expected to be *positive* and *negative*, respectively. We use the ranking-based Spearman correlation rather than Pearson as the relationship between the variables is highly nonlinear (monotonic). The results of Pearson correlation are in Table 7 in the Appendix.

Methods	Brightness	Contrast	Defocus Blur	Elastic Transform	Fog	Frost	Gaussian Blur	Gaussian Noise	Glass Blur
Model ensembles (+)	-0.829	-0.943	-0.486	-0.829	-0.943	-1.000	-0.657	-1.000	-0.714
MC dropout (+)	-1.000	-1.000	-0.600	-0.943	-1.000	-1.000	-0.829	-1.000	-0.486
MCInfoNCE (-)	-1.000	-1.000	-0.429	-0.943	-1.000	-1.000	-0.086	-1.000	-0.714
Ours (-)	-1.000	-1.000	-0.429	-0.943	-1.000	-1.000	-0.771	-0.600	-0.771
	Impulse Noise	JPEG Comp.	Motion Blur	Pixelate	Saturate	Snow	Spatter	Speckle Noise	Zoom Blur
Model ensembles (+)	-1.000	-1.000	-0.943	-1.000	-0.371	-0.829	-0.829	-1.000	-0.522
MC dropout (+)	-1.000	-1.000	-1.000	-1.000	-0.543	-0.830	-0.829	-1.000	-0.714
MCInfoNCE (-)	-0.943	-1.000	-0.943	-0.829	-0.371	-0.600	-0.829	-1.000	0.600
Ours (-)	-0.943	-1.000	-0.943	-0.943	-0.714	-0.943	-0.829	-1.000	-0.943

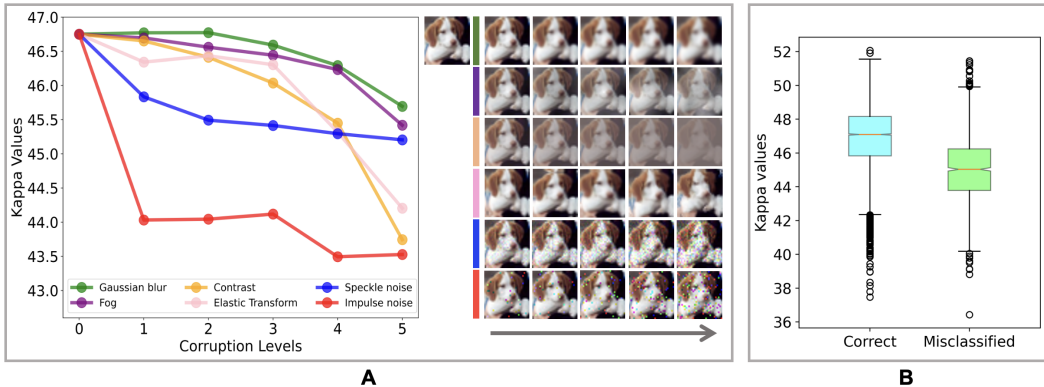


Figure 2: **A.** Decreasing κ implies less concentration and therefore more uncertainty in the representation (*left*). The associated image corruption is from mild to severe (*right*). **B.** The two groups of kappa values (i.e., correctly classified and misclassified) from the test set are significantly different.

Optimization. Following the *SimCLR* configuration, our data augmentation includes random cropping, resizing, color jittering, and horizontal flipping. We train all models on CIFAR-10’s training set for 1000 epochs to quantify corruption levels. Hyper-parameters λ_{align} and λ_{reg} are adjusted for optimal training loss and stability, with λ_{reg} fixed at 0.005 across experiments due to observed training stability. The λ_{align} parameter, dictating alignment loss strength, inversely affects representation discriminativeness and, if increased, may cause training instability. A practical approach involves starting with a low value, like 0.01, and incrementally adjusting up to a saturation point where the total training loss stabilizes; here, λ_{align} is set to 0.05 for *SimCLR*.

4.4 Results

κ captures fine-grained aleatoric uncertainty. We validate the efficacy of our framework on CIFAR-10-C [20], particularly in the context of quantifying fine-grained aleatoric uncertainty. The key focus is on how the concentration parameter κ correlates with various levels of data corruption, providing a probabilistic interpretation of uncertainty in contrastive learning. Table 1 presents the *Spearman* correlation coefficients between κ and different types of data corruption. Notably, the results reveal a strong correlation in scenarios involving brightness, contrast, and defocus blurring, among others. We observe that model ensembles and MC dropout fail to quantify such fine-grained uncertainty for most of the corruptions. By comparing *MC-InfoNCE* and our method, we observe that *MC-InfoNCE* achieves general good-quality estimation but fails to quantify semantics-related corruptions (such as Gaussian blur and Zoom blur). The formulation of *MC-InfoNCE* enforces the κ for the positive pair to be identical. Given that κ correlates with the strength of augmentations, this formulation inherently associates κ with augmentations encountered during training, leading to a κ that is uninformative

Table 2: **AUROC scores for OOD detection.** F_{res} refers to using a k-NN classifier (k=5) based on ResNet-18 features. $F_{res+\kappa}$ denotes the enhancement through the concatenation of κ with the original features.

In-domain	OOD	F_{res}	κ	$F_{res+\kappa}$
CIFAR-10	CIFAR-100	0.9658	0.8162	0.9677
CIFAR-10	MNIST	0.9929	0.6783	0.9937
CIFAR-100	CIFAR-10	0.8653	0.6312	0.8794
CIFAR-100	MNIST	0.9769	0.9390	0.9774
MNIST	CIFAR-10	0.9993	0.9979	0.9999
MNIST	CIFAR-100	0.9998	0.9951	1.0000

Table 3: **Extension to other contrastive learning methods.** ‘Correlation’ refers to the average of Spearman correlations in Tab. 1.

Methods	SimCLR	SimSiam	BYOL	SwaV
Correlation	-0.883	-0.846	-0.835	-0.865

Table 4: **The effect of embedding dimensions** with fixed λ_{align} and λ_{κ} . ‘Correlation’ refers to the average of Spearman correlations in Tab. 1.

Dimension	64	128	256	384
Correlation	-0.768	-0.883	-0.844	-0.901

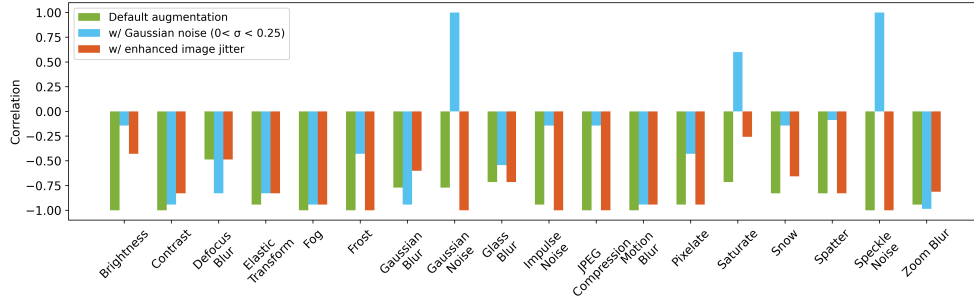


Figure 3: **Additional augmentation degrades the quality of uncertainty estimation for specific types of corruptions.** For instance, introducing Gaussian noise during training causes the correlation with both Gaussian and Speckle noise to shift from negative to positive.

for unseen image corruptions. Our approach ensures κ is dependent on the data and *explicitly* learns κ through interaction with their representations. Figure 2(A) offers a visual interpretation of these correlations. It clearly illustrates how the model’s uncertainty estimation becomes more pronounced as the data corruption increases, showcasing the sensitivity of our framework in dynamically uncertain environments.

κ enables failure analysis. To empirically validate the model’s potential in failure analysis, we analyzed the outcome of the CIFAR-10 test set, which includes 10,000 samples. We divided the predictions into two groups: correctly classified (8,554 κ values) and misclassified (1,446 κ values). The distribution of the two groups is shown in Figure 2(B). Through bootstrapping (50 iterations, each with 100 randomly sampled observations) and applying the Mann-Whitney U test, we sought to robustly compare κ values between the two groups. Our analysis yielded p-values ranging from 6.42×10^{-20} to 1.15×10^{-6} , which strongly suggests a meaningful difference in κ values between correctly and incorrectly classified samples, indicating the model’s potential in failure detection within practical settings.

κ enhances OOD detection. Since κ captures inherent characteristics of the data, it may manifest as epistemic uncertainty. The efficacy of κ as a self-supervised image feature to *enhance* OOD detection methods is evident from the results presented in Table 2, showcasing consistently superior AUROC values by a simple concatenation with existing features. When compared against *ResNet* feature-based baselines derived from supervised learning approaches as discussed in [36] – the addition of κ consistently enhances performance. This improvement highlights κ ’s capacity to capture aleatoric uncertainty that varied between dataset distributions, thereby validating its utility in strengthening OOD detection methods.

κ partially reflects internal augmentations. It is known that internal data augmentation during training enables models to learn invariance to those augmentations. Yet, how the concentration parameter κ reacts to such augmentations, remains unexplored. We add two types of data augmentations one at a time to test the response of κ . Initially, as evidenced by the green bars in Figure 3, the default data augmentations do not weaken the sensitivity of κ . Further introducing Gaussian noise ($\sigma < 0.25$) into the data augmentation pipeline allows the model to adjust effectively, making κ less sensitive to both Gaussian and speckle noise, as indicated by the blue bars. Furthermore, despite the default augmentation

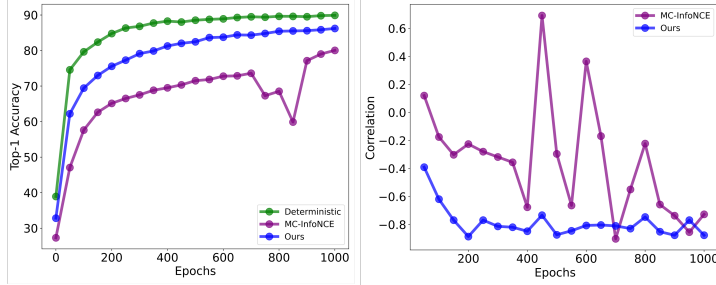


Figure 4: **Left:** Comparison of top-1 classification accuracy on the downstream task over the 1000 training epochs. The deterministic approach represents the original *SimCLR* approach that learns a one-to-one mapping from an image to a representation. **Right:** Comparison of correlation between κ and levels of data corruption (i.e., uncertainty estimation quality) over the 1000 training epochs.

regime, enhancing the image color jittering including brightness (0.3→0.4), contrast (0.3→0.4), saturation (0.3→0.4), and hue ($p = 0.2 \rightarrow p = 0.3$), κ continues to be reactive to these changes. However, intensifying these augmentations leads to significant shifts in the correlations associated with brightness and similar aspects, highlighted by the ■ bars. This suggests the existence of a ‘saturation point,’ beyond which further augmentation fails to meaningfully influence κ ’s assessment of uncertainty. Consequently, to preserve κ ’s efficacy in uncertainty quantification, our framework advises against the use of overly strong augmentations.

Integrating uncertainty without losing much discriminativeness. Our framework not only models aleatoric uncertainty but also maintains the discriminativeness inherent in contrastive learning models. An analysis depicted on the left panel of Figure 4 compares the top-1 classification accuracy on the CIFAR-10 test set and the quality of uncertainty estimation across 1000 training epochs. Despite a modest performance decrease (2%) compared to the deterministic approach, our method exhibits training stability and surpasses the accuracy of the MC sampling-based method [29], demonstrating our model’s effectiveness. Furthermore, the right panel of Figure 4 showcases the consistent performance of our framework in uncertainty estimation. Notably, even in the early stage of training (at the epoch of 200), our model provides high-quality uncertainty estimations.

Adaptability to different methods and dimensions. We adapt our framework to other established contrastive learning methods such as *SimSiam* [7], *BYOL* [14], and *SwaV* [4]), in a manner of adapting to *SimCLR*. Table 3 demonstrates our framework’s versatility, particularly with *SimSiam* and *BYOL*, which train using only positive pairs. As shown in Table 4, the compatibility of our framework different dimensions of the embedding space further attests to its adaptability. More discussions on the results are in the Appendix.

5 Discussion

The findings from this work demonstrate the potential of the concentration parameter κ in uncertainty estimation, failure analysis, and OOD detection. The efficacy of κ in capturing uncertainty, as demonstrated across various datasets and analyses, highlights its applicability in diverse scenarios. However, the scalability of κ in more complex or uncontrolled environments [52, 34] remains for future work. Further investigation into the integration of κ with other OOD detection methodologies, and validation on new application domains (such as healthcare) could yield further advancements.

While the results presented herein are promising, this work has its limitations, which nevertheless, open avenues for future research. Pursuing more sophisticated methods to manage $C_n(\kappa)$ could not only enhance the model’s efficacy but also contribute to the broader discourse on probabilistic modeling. Additionally, the exploration of alternative approximations and reparametrization techniques for κ [23] could yield deeper insights into the delicate interplay between the probabilistic and deterministic components of contrastive learning. In this study, we employ κ primarily for estimating *aleatoric* uncertainty. However, we acknowledge the importance of capturing accurate epistemic uncertainty in the models, to reflect how well the representations are learned in the data-scarcity scenario. We see possible future extensions to incorporate Bayesian inference methods to address this aspect. Furthermore, the extension of our framework to non-contrastive methods, such as MAE

[16] and larger models (as features are in higher dimensions), and the applications to other types of data, including time series, audio, and text, present exciting challenges.

Potential broader impact. Our work introduces a new framework for integrating uncertainty estimation into contrastive learning, with significant implications for critical applications such as autonomous driving and medical diagnosis. This advancement supports the development of transparent and accountable AI systems [26], enhancing decision-making quality by providing clearer insights into the model’s confidence levels. Improving uncertainty estimation helps mitigate risks, especially in high-stakes environments, by alerting users when prediction confidence is low. It is crucial to continuously address potential data biases and validate the model against diverse scenarios to ensure reliability. By making AI decisions more interpretable and demonstrating effective ambiguity handling, our approach builds trust among users for widespread adoption. Future research will focus on integrating this method with other tasks (e.g., classification and segmentation) across various domains, promoting robustness and reliability.

References

- [1] Shekoofeh Azizi, Basil Mustafa, Fiona Ryan, Zachary Beaver, Jan Freyberg, Jonathan Deaton, Aaron Loh, Alan Karthikesalingam, Simon Kornblith, Ting Chen, et al. Big self-supervised models advance medical image classification. In *Proceedings of the IEEE/CVF international conference on computer vision*, pages 3478–3488, 2021.
- [2] Philip Bachman, R Devon Hjelm, and William Buchwalter. Learning representations by maximizing mutual information across views. *Advances in neural information processing systems*, 32, 2019.
- [3] Arindam Banerjee, Inderjit S Dhillon, Joydeep Ghosh, Suvrit Sra, and Greg Ridgeway. Clustering on the unit hypersphere using von mises-fisher distributions. *Journal of Machine Learning Research*, 6(9), 2005.
- [4] Mathilde Caron, Ishan Misra, Julien Mairal, Priya Goyal, Piotr Bojanowski, and Armand Joulin. Unsupervised learning of visual features by contrasting cluster assignments. *Advances in neural information processing systems*, 33:9912–9924, 2020.
- [5] Mathilde Caron, Hugo Touvron, Ishan Misra, Hervé Jégou, Julien Mairal, Piotr Bojanowski, and Armand Joulin. Emerging properties in self-supervised vision transformers. In *Proceedings of the IEEE/CVF international conference on computer vision*, pages 9650–9660, 2021.
- [6] Hansheng Chen, Yuyao Huang, Wei Tian, Zhong Gao, and Lu Xiong. Monorun: Monocular 3d object detection by reconstruction and uncertainty propagation. In *Proceedings of the IEEE/CVF Conference on Computer Vision and Pattern Recognition*, pages 10379–10388, 2021.
- [7] Ting Chen, Simon Kornblith, Mohammad Norouzi, and Geoffrey Hinton. A simple framework for contrastive learning of visual representations. In *International conference on machine learning*, pages 1597–1607. PMLR, 2020.
- [8] Xinlei Chen and Kaiming He. Exploring simple siamese representation learning. In *Proceedings of the IEEE/CVF conference on computer vision and pattern recognition*, pages 15750–15758, 2021.
- [9] Tim R. Davidson, Luca Falorsi, Nicola De Cao, Thomas Kipf, and Jakub M. Tomczak. Hyper-spherical variational auto-encoders. *arXiv preprint arXiv:1804.00891*, 2018.
- [10] Ronald A. Fisher. Dispersion on a sphere. *Proceedings of the Royal Society of London. Series A. Mathematical and Physical Sciences*, 217(1130):295–305, 1953.
- [11] Yarin Gal et al. Uncertainty in deep learning. 2016.
- [12] Yarin Gal and Zoubin Ghahramani. Dropout as a bayesian approximation: Representing model uncertainty in deep learning. in *International Conference on Machine Learning (ICML)*, 2016.
- [13] Songwei Ge, Shlok Mishra, Simon Kornblith, Chun-Liang Li, and David Jacobs. Hyperbolic contrastive learning for visual representations beyond objects. In *Proceedings of the IEEE/CVF Conference on Computer Vision and Pattern Recognition*, pages 6840–6849, 2023.
- [14] Jean-Bastien Grill, Florian Strub, Florent Altché, Corentin Tallec, Pierre Richemond, Elena Buchatskaya, Carl Doersch, Bernardo Avila Pires, Zhaohan Guo, Mohammad Gheshlaghi Azar,

- et al. Bootstrap your own latent—a new approach to self-supervised learning. *Advances in neural information processing systems*, 33:21271–21284, 2020.
- [15] Paul Hager, Martin J Menten, and Daniel Rueckert. Best of both worlds: Multimodal contrastive learning with tabular and imaging data. In *Proceedings of the IEEE/CVF Conference on Computer Vision and Pattern Recognition*, pages 23924–23935, 2023.
- [16] Kaiming He, Xinlei Chen, Saining Xie, Yanghao Li, Piotr Dollár, and Ross Girshick. Masked autoencoders are scalable vision learners. In *Proceedings of the IEEE/CVF conference on computer vision and pattern recognition*, pages 16000–16009, 2022.
- [17] Kaiming He, Haoqi Fan, Yuxin Wu, Saining Xie, and Ross Girshick. Momentum contrast for unsupervised visual representation learning. In *Proceedings of the IEEE/CVF conference on computer vision and pattern recognition*, pages 9729–9738, 2020.
- [18] Kaiming He, Xiangyu Zhang, Shaoqing Ren, and Jian Sun. Deep residual learning for image recognition. In *Proceedings of the IEEE conference on computer vision and pattern recognition*, pages 770–778, 2016.
- [19] Dan Hendrycks and Thomas Dietterich. Benchmarking neural network robustness to common corruptions and perturbations. In *International Conference on Learning Representations*, 2018.
- [20] Dan Hendrycks and Thomas Dietterich. Benchmarking neural network robustness to common corruptions and perturbations. *arXiv preprint arXiv:1903.12261*, 2019.
- [21] Gao Huang, Yixuan Li, Geoff Pleiss, Zhuang Liu, John E Hopcroft, and Kilian Q Weinberger. Snapshot ensembles: Train 1, get m for free. In *International Conference on Learning Representations*, 2016.
- [22] Kim-Celine Kahl, Carsten T Lüth, Maximilian Zenk, Klaus Maier-Hein, and Paul F Jaeger. Val-ues: A framework for systematic validation of uncertainty estimation in semantic segmentation. *arXiv preprint arXiv:2401.08501*, 2024.
- [23] Shogo Kato and Shinto Eguchi. Robust estimation of location and concentration parameters for the von mises–fisher distribution. *Statistical Papers*, 57:205–234, 2016.
- [24] Berk Kaya, Suryansh Kumar, Carlos Oliveira, Vittorio Ferrari, and Luc Van Gool. Uncertainty-aware deep multi-view photometric stereo. In *Proceedings of the IEEE/CVF Conference on Computer Vision and Pattern Recognition*, pages 12601–12611, 2022.
- [25] Alex Kendall and Yarin Gal. What uncertainties do we need in bayesian deep learning for computer vision? *Advances in neural information processing systems*, 30, 2017.
- [26] Been Kim and Finale Doshi-Velez. Machine learning techniques for accountability. *AI Magazine*, 42(1):47–52, 2021.
- [27] Durk P Kingma, Tim Salimans, and Max Welling. Variational dropout and the local reparameterization trick. *Advances in neural information processing systems*, 28, 2015.
- [28] Michael Kirchhof et al. A non-isotropic probabilistic take on proxy-based deep metric learning. In *European Conference on Computer Vision*, Cham, 2022. Springer Nature Switzerland.
- [29] Michael Kirchhof, Enkelejda Kasneci, and Seong Joon Oh. Probabilistic contrastive learning recovers the correct aleatoric uncertainty of ambiguous inputs. *arXiv preprint arXiv:2302.02865*, 2023.
- [30] Alex Krizhevsky, Geoffrey Hinton, et al. Learning multiple layers of features from tiny images. 2009.
- [31] Johnson Kuan and Jonas Mueller. Back to the basics: Revisiting out-of-distribution detection baselines. *arXiv preprint arXiv:2207.03061*, 2022.
- [32] Yann LeCun. The mnist database of handwritten digits. <http://yann.lecun.com/exdb/mnist/>, 1998.
- [33] Weiyang Liu, Yandong Wen, Zhiding Yu, Ming Li, Bhiksha Raj, and Le Song. Sphereface: Deep hypersphere embedding for face recognition. In *Proceedings of the IEEE conference on computer vision and pattern recognition*, pages 212–220, 2017.
- [34] Haodong Lu, Dong Gong, Shuo Wang, Jason Xue, Lina Yao, and Kristen Moore. Learning with mixture of prototypes for out-of-distribution detection. *arXiv preprint arXiv:2402.02653*, 2024.

- [35] James T Meech and Phillip Stanley-Marbell. An algorithm for sensor data uncertainty quantification. *IEEE Sensors Letters*, 6(1):1–4, 2021.
- [36] Yifei Ming, Yiyu Sun, Ousmane Dia, and Yixuan Li. How to exploit hyperspherical embeddings for out-of-distribution detection? In *The Eleventh International Conference on Learning Representations*, 2022.
- [37] Miguel Monteiro, Loïc Le Folgoc, Daniel Coelho de Castro, Nick Pawlowski, Bernardo Marques, Konstantinos Kamnitsas, Mark van der Wilk, and Ben Glocker. Stochastic segmentation networks: Modelling spatially correlated aleatoric uncertainty. *Advances in neural information processing systems*, 33:12756–12767, 2020.
- [38] Vinod Nair and Geoffrey E. Hinton. Rectified linear units improve restricted boltzmann machines. In *Proceedings of the 27th International Conference on International Conference on Machine Learning*, pages 807–814. Omnipress, 2010.
- [39] Maximilian Nickel and Douwe Kiela. Poincaré embeddings for learning hierarchical representations. In *Advances in Neural Information Processing Systems (NeurIPS)*, 2017.
- [40] Brett D Roads and Bradley C Love. Enriching imagenet with human similarity judgments and psychological embeddings. In *Proceedings of the IEEE/CVF conference on computer vision and pattern recognition*, pages 3547–3557, 2021.
- [41] Tyler R Scott, Andrew C Gallagher, and Michael C Mozer. von mises-fisher loss: An exploration of embedding geometries for supervised learning. In *Proceedings of the IEEE/CVF International Conference on Computer Vision*, pages 10612–10622, 2021.
- [42] Yichun Shi and Anil K. Jain. Probabilistic face embeddings. In *Proceedings of the IEEE/CVF International Conference on Computer Vision*, 2019.
- [43] Yonglong Tian, Dilip Krishnan, and Phillip Isola. Contrastive multiview coding. In *Computer Vision—ECCV 2020: 16th European Conference, Glasgow, UK, August 23–28, 2020, Proceedings, Part XI 16*, pages 776–794. Springer, 2020.
- [44] Uddeshya Upadhyay, Shyamgopal Karthik, Massimiliano Mancini, and Zeynep Akata. Problm: Probabilistic adapter for frozen vision-language models. In *Proceedings of the IEEE/CVF International Conference on Computer Vision*, pages 1899–1910, 2023.
- [45] Aaron van den Oord, Yazhe Li, and Oriol Vinyals. Representation learning with contrastive predictive coding. *arXiv preprint arXiv:1807.03748*, 2018.
- [46] Feng Wang and Huaping Liu. Understanding the behaviour of contrastive loss. In *Proceedings of the IEEE/CVF conference on computer vision and pattern recognition*, pages 2495–2504, 2021.
- [47] Feng Wang, Xiang Xiang, Jian Cheng, and Alan Loddon Yuille. Normface: L2 hypersphere embedding for face verification. In *Proceedings of the 25th ACM international conference on Multimedia*, pages 1041–1049, 2017.
- [48] Tongzhou Wang and Phillip Isola. Understanding contrastive representation learning through alignment and uniformity on the hypersphere. In *International Conference on Machine Learning*, pages 9929–9939. PMLR, 2020.
- [49] George Neville Watson. *A treatise on the theory of Bessel functions*, volume 2. The University Press, 1922.
- [50] Jiacheng Xu and Greg Durrett. Spherical latent spaces for stable variational autoencoders. In *Proceedings of the 2018 Conference on Empirical Methods in Natural Language Processing*. Association for Computational Linguistics, 2018.
- [51] Jure Zbontar, Li Jing, Ishan Misra, Yann LeCun, and Stéphane Deny. Barlow twins: Self-supervised learning via redundancy reduction. In *International Conference on Machine Learning*, pages 12310–12320. PMLR, 2021.
- [52] Jingyang Zhang, Jingkang Yang, Pengyun Wang, Haoqi Wang, Yueqian Lin, Haoran Zhang, Yiyu Sun, Xuefeng Du, Kaiyang Zhou, Wayne Zhang, et al. Openood v1. 5: Enhanced benchmark for out-of-distribution detection. *arXiv preprint arXiv:2306.09301*, 2023.

Appendix

A Description of corruption types from CIFAR-10-C

Table 5: Types of image corruption and their descriptions from CIFAR-10-C [20].

Type	Description
Gaussian Noise	Often occurs in conditions of poor lighting and adds random fluctuations to pixel values.
Shot Noise	Represents electronic noise emerging due to the inherent discreteness of light, leading to pixel-level variability.
Impulse Noise	Similar to the color version of salt-and-pepper noise, arises from bit errors and manifests as isolated pixel outliers.
Defocus Blur	Occurs when images are not in sharp focus, resulting in a slight blurriness.
Frosted Glass Blur	Resembles the effect seen through frosted glass surfaces, introducing a diffuse and obscured appearance.
Motion Blur	Created by rapid camera movements, causing objects to appear streaked or elongated.
Zoom Blur	Results from quickly moving the camera towards an object, causing a radial blurring effect.
Snow	An obstruction in visual perception, characterized by the presence of white or colored specks in the image.
Frost	Ice crystals on lenses or windows disrupt image clarity, leading to a frosted appearance.
Fog	Cloaks objects in images, simulated using the diamond-square algorithm, resulting in a hazy and obscured view.
Brightness	Affected by variations in daylight intensity, causing overall illumination changes.
Contrast	Depends on lighting conditions and the object's inherent color, leading to alterations in image contrast.
Elastic Transformations	Lead to stretching or contracting of small regions in an image, distorting local features.
Pixelation	A consequence of enlarging a low-resolution image, causing blocky artifacts due to limited pixel information.
JPEG Compression	A lossy method that reduces image size and can introduce artifacts such as blockiness and blurring.

B Analysis of the Gradients from $\mathcal{L}_{\text{align}}$

The gradient of $\mathcal{L}_{\text{align}}$ w.r.t. μ_1 . Given L_a in Eq. 9, the gradient of its log w.r.t. μ_1 can be obtained by differentiating the loss function w.r.t. μ_1 . Its gradient can be expanded as follows:

$$\nabla_{\mu_1} \log L_a = \nabla_{\mu_1} [\kappa_1 \cdot \cos(\theta) + \kappa_2 \cdot \cos(\theta)] \quad (13)$$

Now, $\cos(\theta) = \mu_1^T \mu_2$, and its gradient w.r.t. μ_1 is μ_2 . Plug this into the gradient of $\mathcal{L}_{\text{align}}$, we get:

$$\nabla_{\mu_1} \mathcal{L}_{\text{align}} = -\lambda_{\text{align}} \cdot (\kappa_1 \mu_2 + \kappa_2 \mu_2) \quad (14)$$

This gradient aligns μ_1 towards μ_2 , similar to those with existing contrastive losses. More importantly, however, the *strength* of this alignment effect is *controlled* by the estimated concentration parameters κ_1 and κ_2 (i.e., the estimated uncertainties) of both μ_1 and μ_2 . Smaller κ 's indicate more uncertainties and lead to looser alignment. Compared with conventional contrastive losses which naively align positive pairs regardless of the severity of corruptions in the input, our $\mathcal{L}_{\text{align}}$ yields a more flexible latent space that is aware of the severity of corruptions in the input.

The gradient of $\mathcal{L}_{\text{align}}$ w.r.t. κ_1 . Similarly, we can compute the gradient of $\mathcal{L}_{\text{align}}$ w.r.t. κ_1 as follows:

$$\nabla_{\kappa_1} \mathcal{L}_{\text{align}} = -\lambda_{\text{align}} \cdot \mu_1^T \mu_2 \quad (15)$$

Eq. 15 implies that a closer cosine distance between μ_1 and μ_2 encourages a stronger increase in κ_1 , indicating reduced uncertainty. The increasing effect on κ_1 weakens as the distance between μ_1 and μ_2 grows. Meanwhile, when the angle between μ_1 and μ_2 surpasses $\frac{\pi}{2}$, the gradient encourages a reduction in κ_1 instead, hence an increase in predicted uncertainty. Of note, κ 's would not grow uninformatively large as they are bounded by the ℓ_2 regularization (Eq. 11) at the same time.

C Discussion on Results of Different Network Complexity, Embedding Dimensions, and Learning Frameworks

Table 6 further demonstrates the versatility of our approach across different network architectures, including *ResNet18*, *ResNet34*, and *ResNet50*. Our method consistently achieves strong correlation coefficients, illustrating that the introduction of κ does not compromise the discriminative nature of the embeddings. Instead, it enriches the model’s representation by providing a probabilistic dimension that captures uncertainty directly related to the data’s intrinsic characteristics.

The compatibility of our framework with established contrastive learning methods, such as *SimSiam* [7], *BYOL* [14], and *SwaV* [4], further attests to its adaptability. Table 3 demonstrates our framework’s versatility, particularly with *SimSiam* and *BYOL*, which train using only positive pairs. Across these methods, our approach consistently achieves strong correlation coefficients, underscoring the substantial promise of our design. This extension is not merely a testament to the flexibility of our approach but also promises to broaden the applicability of contrastive learning models in handling diverse applications.

In Table 4, we investigate the effect of embedding dimensions on κ ’s capability to quantify uncertainty. With embedding dimensions set at 64, 128, 256, and 384, our framework demonstrates a nuanced performance variation, indicated by the correlation coefficients -0.768, -0.883, -0.844, and -0.901, respectively. The optimal performance at 128 and 384 dimensions suggests a critical balance between dimensionality and the model’s ability to effectively capture uncertainty.

Table 6: **The effect of network complexity** with fixed λ_{align} , λ_{κ} , and number of embedding dimension (dim. = 128). ‘Correction’ refers to the average of 18 Spearman correlations from the types of corruption listed in Table 1.

Architecture	ResNet18	ResNet34	ResNet50
Correlation	-0.908	-0.876	-0.883

Table 7: **Pearson correlation between kappa values and the levels of corruption.** As the severity of corruption increases, the concentration parameter kappa decreases, implying higher uncertainty in the representations. + and - indicate that the correlation are expected to *positive* and *negative*, respectively.

Methods	Brightness	Contrast	Defocus Blur	Elastic Transform	Fog	Frost	Gaussian Blur	Gaussian Noise	Glass Blur
Model ensembles (+)	-0.791	-0.891	-0.687	-0.822	-0.655	-0.986	-0.776	-0.919	-0.685
MC dropout (+)	-0.913	-0.882	-0.818	-0.862	-0.920	-0.984	-0.878	-0.916	-0.664
MCInfoNCE (-)	-0.915	-0.937	-0.525	-0.850	-0.913	-0.969	-0.289	-0.818	-0.685
Ours (-)	-0.893	-0.876	-0.802	-0.892	-0.901	-0.949	-0.845	-0.737	-0.770
	Impulse Noise	JPEG Comp.	Motion Blur	Pixelate	Saturate	Snow	Spatter	Speckle Noise	Zoom Blur
Model ensembles (+)	-0.993	-0.918	-0.973	-0.990	-0.350	-0.832	-0.846	-0.976	-0.551
MC dropout (+)	-0.996	-0.869	-0.987	-0.972	-0.541	-0.835	-0.840	-0.976	-0.825
MCInfoNCE (-)	-0.904	-0.869	-0.971	-0.850	-0.462	-0.741	-0.892	-0.923	0.648
Ours (-)	-0.927	-0.959	-0.980	-0.959	-0.563	-0.877	-0.887	-0.881	-0.892

D MC-InfoNCE with the *SimCLR* contrastive loss

```

1 from torch import nn
2 import torch
3 from vmf_sampler import VonMisesFisher
4 from utils_mc import pairwise_cos_sims, pairwise_l2_dists,
   log_vmf_norm_const
5 import torch
6 import torch.nn as nn
7
8 class MCSimCLR(nn.Module):
9     def __init__(self, kappa_init=16, n_samples=64, temperature=0.5,
10        device=torch.device('cuda:0')):
11         super().__init__()
12         self.n_samples = n_samples
13         self.kappa = torch.nn.Parameter(torch.ones(1, device=device) *
14            kappa_init, requires_grad=True)
15         self.temperature = temperature
16
17     def forward(self, mu1, kappa1, mu2, kappa2):
18         # Draw samples from the von Mises-Fisher distribution
19         samples1 = VonMisesFisher(mu1, kappa1).rsample(torch.Size([self.
20            n_samples]))
21         samples2 = VonMisesFisher(mu2, kappa2).rsample(torch.Size([self.
22            n_samples]))
23         # Concatenate positive samples for contrastive loss calculation
24         samples = torch.cat([samples1, samples2], dim=1) # [n_MC, 2 *
25            batch, dim]
26         # Compute similarity matrix
27         sim_matrix = torch.exp(torch.matmul(samples, samples.transpose(2,
28            1)) / self.temperature)
29         # Create mask to zero-out self-similarities (diagonal elements)
30         batch_size = mu1.size(0)
31         mask = ~torch.eye(2 * batch_size, device=sim_matrix.device, dtype
32            =bool).repeat(self.n_samples, 1, 1)
33         sim_matrix = sim_matrix.masked_select(mask).view(self.n_samples,
34            2 * batch_size, -1)
35         # Similarities for the positive pairs)
36         pos_sim = torch.exp(torch.sum(samples1 * samples2, dim=2) / self.
37            temperature)
38         pos_sim = torch.cat([pos_sim, pos_sim], dim=1) #Duplicate pos_sim
39         loss = -torch.log(pos_sim / sim_matrix.sum(dim=2))
40         loss = loss.mean()
41         return loss

```

E Architecture

```
1 import torch
2 import torch.nn as nn
3 import torch.nn.functional as F
4 from torchvision.models import resnet50, resnet18, resnet34
5 class ProbabilisticModel(nn.Module):
6     def __init__(self, feature_dim=128):
7         super(ProbabilisticModel, self).__init__()
8
9         # Define the layers of the ResNet model
10        self.f = []
11        for name, module in resnet50().named_children():
12            if name == 'conv1':
13                module = nn.Conv2d(3, 64, kernel_size=3, stride=1,
padding=1, bias=False)
14            if not isinstance(module, nn.Linear) and not isinstance(
module, nn.MaxPool2d):
15                self.f.append(module)
16            self.f = nn.Sequential(*self.f)
17
18        # Projection head for feature
19        self.g = nn.Sequential(
20            nn.Linear(2048, 512, bias=False),
21            nn.BatchNorm1d(512),
22            nn.ReLU(inplace=True),
23            nn.Linear(512, feature_dim, bias=True)
24        )
25        # Additional layer for kappa (concentration parameter)
26        self.kappa_head = nn.Sequential(
27            nn.Linear(2048, 512, bias=False),
28            nn.BatchNorm1d(512),
29            nn.ReLU(inplace=True),
30            nn.Linear(512, 1, bias=True) # Outputs kappa for each sample
31        )
32
33    def forward(self, x):
34        x = self.f(x)
35        feature = torch.flatten(x, start_dim=1)
36        out = self.g(feature)
37        kappa = self.kappa_head(feature) # Compute kappa for each sample
38        # Normalize the feature vector and return it with variance and
kappa
39        return F.normalize(out, dim=-1), F.softplus(kappa.squeeze(-1))
40
```

F Training

```
1
2 # train for one epoch to learn the mean vector mu and kappa
3 def train(net, data_loader, train_optimizer):
4     net.train()
5     total_loss, total_num, train_bar = 0.0, 0, tqdm(data_loader)
6     epsilon = 1e-6 # Small constant for numerical stability
7     align_strength = 0.05 # Hyperparameter to regularize the embedding
8     kappa_reg_strength = 0.005 # Hyperparameter for the regularization
9     simclr_strength = 1 # Hyperparameter for the strength of SimCLR loss
10
11     for pos_1, pos_2, target in train_bar:
12         pos_1, pos_2 = pos_1.to(device), pos_2.to(device)
13
14         mean_1, kappa_1 = net(pos_1)
15         mean_2, kappa_2 = net(pos_2)
16
17         # Compute the embedding alignment loss component
18         alignment = torch.exp(kappa_1 * F.cosine_similarity(mean_1,
19 mean_2, dim=1)) + \
20         kappa_2 * F.cosine_similarity(mean_1, mean_2, dim=1))
21         align_loss = align_strength * (-torch.log(alignment + epsilon)).
22         mean()
23
24         # Compute the regularization loss for kappa (L2 norm)
25         kappa_reg_loss = kappa_reg_strength * (torch.mean(kappa_1 ** 2) +
26 \
27         torch.mean(kappa_2 ** 2))
28
29         # Compute SimCLR contrastive loss
30         out = torch.cat([mean_1, mean_2], dim=0)
31         sim_matrix = torch.exp(torch.mm(out, out.t().contiguous()) /
32 temperature)
33         mask = (torch.ones_like(sim_matrix) - torch.eye(2 * batch_size, \
34 device=sim_matrix.device)).bool()
35         sim_matrix = sim_matrix.masked_select(mask).view(2 * batch_size,
36 -1)
37         pos_sim = torch.exp(torch.sum(mean_1 * mean_2, dim=-1) /
38 temperature)
39         pos_sim = torch.cat([pos_sim, pos_sim], dim=0)
40         contrastive_loss = simclr_strength * \
41         (-torch.log(pos_sim / sim_matrix.sum(dim=-1))).mean()
42
43         # Compute the final loss
44         loss = align_loss + contrastive_loss + kappa_reg_loss
45
46         # Backward and optimize
47         train_optimizer.zero_grad()
48         loss.backward()
49         train_optimizer.step()
```